Understanding the Effects of Manganese and Zinc Promoters on Ferrite Catalysts for CO₂ Hydrogenation to Hydrocarbons through Colloidal Nanocrystals

Chih-Jung Chen^{a,#}, Jinwon Oh^{b,#}, An-Chih Yang^a, Chengshuang Zhou^a, Gennaro Liccardo^{a,c}, Shradha Sapru^d, and Matteo Cargnello^{a,*}

KEYWORDS

CO₂ Hydrogenation, Colloidal Nanoparticles, Ferrite, Promoter, Structural Stabilizers

a Department of Chemical Engineering, Stanford University, Stanford, California 94305, USA

b Department of Materials Science and Engineering, Stanford University, Stanford, California 94305, USA

^C SLAC National Accelerator Laboratory, Menlo Park, California 94025, USA

d Department of Chemistry, Stanford University, Stanford, California 94305, USA

^{*}These authors equally contributed to this work.

ABSTRACT

CO₂ hydrogenation is a crucial reaction in the pursuit of sustainable fuels and chemicals. Iron-based catalysts, known for their activity, have garnered attention due to their potential, but sintering and still limited performance have encouraged researchers to explore additives and promoters in ferrite phases. Nonetheless, a systematic approach is required to comprehensively understand the roles of the promoters. This study analyzed the catalytic performance of colloidal ferrite nanocrystals added with manganese and zinc additives for CO₂ hydrogenation. The precise control afforded by colloidal synthesis enabled the fine-tuning of catalyst properties. The findings revealed that both manganese and zinc additives effectively counteracted sintering effects, leading to decreased particle sizes after the reaction. The contribution of manganese additives to promoting CO₂ hydrogenation performance was however limited, resulting in lower CO₂ conversion and reduced selectivity towards C₂₊ hydrocarbons compared to the bare ferrite catalyst. Notably, the introduction of zinc instead yielded a dual benefit of improved catalytic activity and selectivity. This enhancement was attributed to enhanced reducibility that facilitated the formation of carbide-like phases, considered the active species.

1. Introduction

Global energy demand continues to grow, and it is estimated to increase by 48% between 2012 and 2040. Despite the increased utilization of renewable and carbon-free energy sources, the International Energy Agency (IEA) has highlighted that the largest proportion of our energy needs is still being met through the consumption of fossil fuels. Consequently, this heavy reliance on fossil fuels has led to a significant rise in carbon emissions, resulting in an increase in atmospheric CO₂ concentration from 280 to 406 ppm over the past 150 years. The severe environmental consequences stemming from this situation, including climate change, the greenhouse effect, and global warming, necessitate the exploration of alternative approaches to mitigate CO₂ emissions. In response, various strategies for CO₂ conversion through chemical processes have been extensively researched over the past decade. Among these approaches, the CO₂ hydrogenation reaction utilizing heterogeneous catalysts stands out, as it offers a promising avenue to curtail carbon emissions while concurrently reducing our dependence on fossil fuels.

Initial studies in CO₂ hydrogenation predominantly focused on generating single-carbon (C₁) products like CO, CH₄, or CH₃OH. However, a more impactful approach involves the conversion of CO₂ into liquid hydrocarbons, which not only enhances energy density but also presents a feasible substitute for existing fossil fuels. To achieve this, thermodynamic considerations dictate the necessity of elevated pressure conditions above atmospheric levels.³ These conditions increase the likelihood of C-C coupling, leading to the production of long-chain hydrocarbons (C₂₊) as opposed to C₁ compounds. Recent advancements have seen the development of CO₂ hydrogenation catalysts under milder pressure conditions, yielding not only light hydrocarbons but also olefins and alcohols.⁴⁻⁶ These products hold significance as key building blocks in the chemical industry.⁷ Hence, conducting CO₂ hydrogenation at moderate pressures yields substantial advantages.

The CO₂ hydrogenation process typically occurs in two successive steps: the reverse water-gas shift (RWGS) reaction initially converts CO₂ to CO, followed by the transformation of CO into hydrocarbons through Fischer-Tropsch synthesis (FTS). Iron-based catalysts have attracted significant attention due to their remarkable selectivity towards long-chain products.⁸⁻¹¹ In this context, the Fe₃O₄ phase serves as the active site for the RWGS step,¹²⁻¹³ while the Hägg iron carbide (χ -Fe₅C₂) phase is speculated to be the active site for hydrocarbon production, especially in the presence of promoters.¹⁴⁻¹⁵ The relative proportion of Fe₃O₄ to χ -Fe₅C₂ phases significantly influences product selectivity, and reducing pre-treatments are typically required before CO₂ hydrogenation. During catalysis, the catalyst phases interact with dissociated oxygen and carbon atoms, leading to the formation of active Fe₃O₄ and χ -Fe₅C₂ species. However, these reduction procedures often induce sintering of the active phase, complicating efforts to establish correlations between catalyst structure and performance.⁸

To mitigate sintering-related issues, manganese or zinc promoters are incorporated into iron-based catalysts to stabilize their structure. Nonetheless, the presence of promoters also impacts catalytic properties. For instance, Liang *et al.* studied Mn-decorated iron catalysts using H₂-temperature programmed reduction (TPR) measurements and noted a gradual shift in the initial reduction peak to lower temperatures with increasing Mn content. This phenomenon was attributed to the conversion of the catalyst main phase from Fe₂O₃ to Fe₃O₄, along with a reduction in particle size. Conversely, Ma's group reported that Mn additives hindered the reducibility of iron catalysts. The Similar conflicting results have also arisen in studies discussing Zn promoters. The Zn promoters have been proposed to function as structural stabilizers, retarding the sintering of iron particles and thereby increasing the availability of the active surfaces. Some research also suggests that Zn promoters form strong interactions with Fe, inhibiting the reduction of iron oxide. However, Cui *et al.* demonstrated that the addition of Zn significantly enhanced the reducibility of iron oxide, as shown by their H₂-TPR results, benefiting the

formation of Fe₃O₄ and metallic Fe.²¹ These contradictory outcomes may arise from the use of conventional preparation methods (such as co-precipitation, impregnation), which simultaneously vary multiple parameters like particle size, size distribution, and composition. This complexity presents a challenge in systematically analyzing the role of promoters in iron catalysts, often leading to ambiguous results.

To address the aforementioned challenges and uncover trends in structure-activity relationships, colloidal catalysts offer a viable solution.²² Colloidal synthesis enables precise control over attributes like size, shape, composition, and surface characteristics, allowing for comprehensive analysis of their impact on catalytic performance. In this study, uniform ferrite colloidal nanocrystals (Fe₃O₄) were synthesized to serve as catalysts for CO₂ hydrogenation. The incorporation of promoters in varying quantities facilitated an assessment of their correlation with catalytic performance, sintering effects, and active phase ratios. These parameters are pivotal in understanding the dynamics of CO₂ hydrogenation and chain growth.¹²⁻¹³ This study provides insights into the influence of additives on ferrite catalysts, shedding light on their potential for enhancing CO₂ hydrogenation efficiency.

2. Experimental Section

2.1 Chemicals and Materials

Manganese (II) acetylacetonate, 1,2-hexadecanediol (90%), 1,2-tetradecanediol (90%), oleic acid (90%), 1-oleylamine (70%) were purchased from Sigma-Aldrich. Iron (III) acetylacetonate (99+%), zinc (II) acetylacetonate (ca. 25% Zn), benzyl ether (99%) and 1-octadecene (90%) were purchased from ACROS Organics. CNTs were purchased from US Research Nanomaterials, Inc. (product number 4306). All chemicals were used as received and without further purification.

2.2 Synthesis of colloidal particles

The parent iron oxide (ferrite) colloidal particles were prepared following previous work with minor modifications.²³ For Fe₃O₄ colloids, iron (III) acetylacetonate (1.2 mmol), 1,2-hexadecanediol (2.4 mmol), 0.26 mL oleic acid (0.8 mmol), 1.28 mL oleylamine (4 mmol), and 1.2 mL benzyl ether were mixed in a three-neck flask. The solution was heated under a N₂ atmosphere and kept at 110 °C, 205 °C, and 295 °C for 1, 1.5, and 1 h, respectively. Afterwards, it was naturally cooled to RT, and separated into two centrifuge tubes. Oleic acid was added to achieve a total solution volume of 15 mL that resulted in particle precipitation, and the particles were recovered by centrifugation at 8500 rpm for 5 min. The supernatant was subsequently discarded, and the precipitates were redisperse in 10 mL hexane for size-selection (see below).

Mn- and Zn-ferrite particles were prepared similarly to the Fe₃O₄ colloids. Iron (III) acetylacetonate and manganese (II) (or zinc (II) acetylacetonate) with Fe:Mn (or Zn) molar ratios of 5:1 and 1:1 (total of 1.2 mmol) were used, respectively. A minor difference was that 1,2-tetradecanediol (2.4 mmol) was utilized to synthesize manganese ferrite rather than 1,2-hexadecanediol. Heating and washing steps were the same

as Fe₃O₄ colloids. It is worth noting that both 1,2-hexadecanediol and 1,2-tetradecanediol can be utilized to prepare iron-based colloids.²³⁻²⁵ These organic ligands are subsequently removed through heat treatment before catalysis, as explained in the section detailing the preparation of supported particles. Additionally, since we observed no differences in morphology or particle size, we can safely disregard any impact on the catalysis from the diol ligands.

2.3 Size selection of colloidal particles

Size selection was performed on the as-synthesized particles to improve size distribution. Oleic acid (10 mL) was added dropwise into the as-prepared colloidal solution under stirring, and centrifuged at 8000 rpm for 10 min. The supernatant with small particles was discarded, and the precipitates were redispersed in 20 mL hexane. Oleic acid (7.5 mL) was added into the above solution under stirring and centrifuged once again at 8000 rpm for 10 min. The precipitate of large particle sizes was removed from the liquid phase. Afterwards, oleic acid was added to the liquid phase from the previous step to achieve a total volume of 30 mL, the particles were precipitated by centrifugation at 8000 rpm for 10 min, and the supernatant was discarded. The precipitate was dispersed in 5 mL hexane and added with 25 mL of ethanol and centrifuged at 8000 rpm for 10 min. Finally, these uniform particles were stored in 5 mL of hexane.

2.4 Preparation of supported particles

The prepared colloids were deposited on carbon nanotubes (CNTs) used as support to carry out the reaction. The method used for the deposition was developed in a previous study. ²⁵ CNTs (200 mg) were added to 10 mL 1-octadecene in a three-neck flask and the mixture was sonicated for 10 min. A colloidal

solution volume to obtain approximately 3 wt. % loading of the particles on CNTs was added into the above suspension, and the flask was degassed for 15 min at 120 °C under vacuum. The dispersion was subsequently heated to 200 °C under a N_2 atmosphere for 30 min. After cooling to room temperature, 40 mL of a hexane:acetone 1:3 mixture was added into the suspension and centrifuged at 8500 rpm for 5 min. This cleaning step was repeated once more, and the catalyst sample was vacuum dried at 80 °C overnight. To remove organic ligands around particles, all supported particles were heated at 700 °C in air for 30 s, 26 before the catalytic performance was measured. To quantify the elements in our catalysts, we employed inductively coupled plasma optical emission spectroscopy (ICP-OES) using a Thermo Scientific ICAP 6300 Duo View Spectrometer. The catalyst powders (approximately 100 mg) were subjected to digestion in a mixture of nitric acid (710 μ L) and hydrochloric acid (660 μ L) for a duration of 10 h. Subsequently, the digested samples were filtered and diluted to a concentration of 5 ppm prior to the analytical measurements.

2.5 Catalytic tests

CO₂ hydrogenation was performed in a custom-made stainless-steel reactor with an internal diameter of 1 cm. The catalyst bed consisted of approximately 100 mg catalyst powder diluted with SiC (~200 mg) through granular mixing, and the solid mixture was sandwiched between two layers of acid-washed quartz (upstream: 300 mg; downstream: 400 mg) in the reactor. Prior to conducting the reaction, the catalysts were reduced at 400 °C in pure H₂ atmosphere at a flow rate of 30 mL min⁻¹ for 3 h. After the pretreatment, the reactor was cooled down to 300 °C. A gas mixture of CO₂:H₂ = 1:3 was used at a flow rate of 10 mL min⁻¹ at a total pressure of 6 bar.

2.6 Structural characterization of materials

Transmission electron microscopy was performed on an FEI Tecnai equipped with an Orius CCD and a Gatan OneView camera operating at 200 kV. The crystallinity and crystal structure were analyzed by an X-ray diffraction analyzer (Bruker D2 PHASER) with Cu K $_{\alpha}$ radiation (λ =1.54178 Å). X-ray photoelectron spectroscopy (XPS) measurements were performed using a PHI VersaProbe 4 with an Al k α source. Powder samples were carefully fixed to a 2 inches platen through double sided conductive tape. No charge compensators were used in the measurements. The spectra were shifted according to a Cu reference sputtered for 2 minutes to obtain metallic Cu. Spectra were obtained with pass energy of 55 eV and a step of 0.05 eV.

3. Results and Discussion

Colloidal synthesis methods were employed in this study to prepare monodisperse ferrite (Fe₃O₄) particles (Fig. 1a and 1f), which served as catalyst precursors for CO₂ hydrogenation. Prior research had successfully demonstrated the controlled synthesis of ferrite nanocrystals with precise control over their size, shape, and composition.²³ To enhance catalytic performance, the ferrite particles were combined with metal (M) promoters, specifically Mn or Zn, leading to distinct M/Fe atomic ratios (Mn_{0.10}Fe_{2.90}O₄, Mn_{0.64}Fe_{2.36}O₄, Zn_{0.19}Fe_{2.81}O₄, and Zn_{0.68}Fe_{2.32}O₄). Notably, the incorporation of these additives during the synthesis process led to broader particle size distributions in contrast to the pure ferrite nanocrystals. For example, in the case of zinc ferrite nanocrystals, the sample displayed two distinct particle size distributions (Fig. S1a). Larger particles exhibited a high Zn/Fe ratio, whereas smaller particles showcased a comparatively lower Zn concentration (Fig. S1b-c). These findings suggest potential disparities in the nucleation processes of Zn and Fe oxides. In response to this observation, it was deemed necessary to implement a particle size selection process in order to isolate particles with homogeneous distributions of Zn and Fe components. To avoid the use of protic anti-solvents like methanol or ethanol, which might remove capping ligands from the particle surfaces and result in particle precipitation, oleic acid was employed as an alternative anti-solvent.²⁷ This approach followed the methodology of previous studies. ^{23,28} Hence, size selection was carried out by adding oleic acid as a precipitant to achieve uniform particle diameter and composition of manganese and zinc ferrite nanocrystals. After undergoing this procedure, the average size of the Mn- and Zn-promoted colloids was reduced to approximately 6-7 nm (Fig. 1 b-e and 1g-j), and the particle size distributions became significantly narrower.

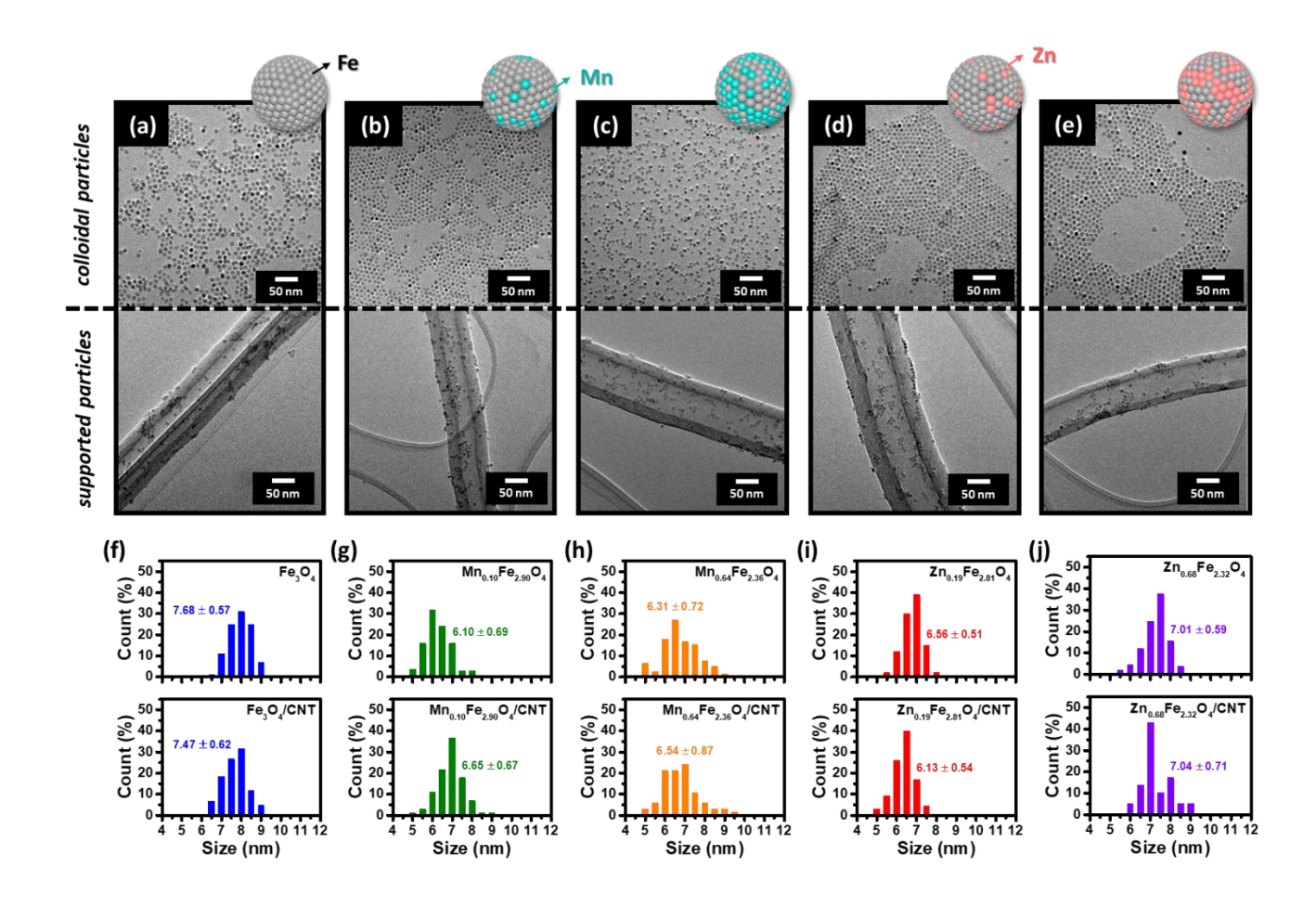


Fig. 1. TEM images of (a) Fe₃O₄, (b) Mn_{0.10}Fe_{2.90}O₄, (c) Mn_{0.64}Fe_{2.36}O₄, (d) Zn_{0.19}Fe_{2.81}O₄, and (e) Zn_{0.68}Fe_{2.32}O₄ colloidal particles and supported particles on carbon nanotubes (CNT). Particle size distributions of (f) Fe₃O₄, (g) Mn_{0.10}Fe_{2.90}O₄, (h) Mn_{0.64}Fe_{2.36}O₄, (i) Zn_{0.19}Fe_{2.81}O₄, and (j) Zn_{0.68}Fe_{2.32}O₄ colloidal and supported particles.

Previous research has elucidated that the distinctive electronic properties and substantial surface area of carbon nanotubes (CNTs) facilitate their use as supports for iron-based catalysts in CO₂ hydrogenation, leading to the generation of catalytically active carbide phases. ¹² Therefore, in the present study, the choice of CNTs as the support was considered crucial for the preparation of highly dispersed and effective catalyst

materials. The particle size distributions of the colloidal catalysts remained consistent after deposition (Fig. 1). Notably, no significant aggregation was observed, underscoring the advantageous role of the CNT support in achieving uniform dispersion of the nanocrystals.

To analyze the crystal structure, crystallinity, and phase purity of the supported catalysts, X-ray diffraction (XRD) was conducted (Fig. 2). The XRD patterns revealed two broad peaks corresponding to the (002) and (100) Miller indices of the CNT support at 2θ values of 26 and 43°, respectively. The diffraction peaks of the ferrite catalyst exhibited positions at ~29.7, 35.2, 53.8, 56.6, and 62.4°, corresponding to the (220), (311), (422), (511), and (440) facets of the Fe₃O₄ phase. A weak peak at \sim 33° was attributed to the (104) crystal plane of α-Fe₂O₃ species. These findings established that the dominant phase within the ferrite nanocrystals was Fe₃O₄, with a minor presence of the Fe₂O₃ phase as a side product possibly resulting from surface oxidation upon exposure to air. Interestingly, the XRD patterns of the Mnand Zn-promoted catalysts closely resembled that of pure ferrite, without discernible zinc oxide or manganese oxide phases. This outcome was in contrast with a study by Zhai and co-workers, where conventional co-precipitated spinel ZnFe₂O₄ exhibited reduced crystallite size. ¹⁹ However, in our case, the XRD peak widths remained similar across all samples, consistent with TEM characterization and with the use of colloidal synthesis (Fig. 1). Notably, upon the introduction of small amounts of promoters to ferrite nanocrystals (Mn_{0.10}Fe_{2.90}O₄ and Zn_{0.19}Fe_{2.81}O₄), the XRD peak intensity of the α-Fe₂O₃ phase diminished. Besides, only peaks related to the Fe₃O₄ phase were observed in the XRD spectra of Mn_{0.64}Fe_{2.36}O₄ and Zn_{0.68}Fe_{2.32}O₄ samples. This observation could be attributed to either a reduced crystallinity of the Fe₂O₃ phase, if present, or an enhanced stabilization of the Fe oxidation state within the spinel structure. To further understand the oxidation states of Fe species on the surface, we performed X-ray photoelectron spectroscopy (XPS) (Fig. S2). In XPS spectra, Zn_{0.68}Fe_{2.32}O₄ is distinctively different from the rest of the samples, being the most oxidized in the Fe region, as the line at 711.7 eV highlights a

peak shift to higher binding energy compared to the other spectra. Similarly, the line at 724 eV that aligns well with peaks for all other samples is clearly off for this sample. While the differences in the other samples are more subtle, pure ferrite does not show a tail past the 728 eV line, suggesting it may be the least oxidized of the samples. Moreover, the clear presence of a satellite peak at the 719.1 eV line suggests the coexistence of Fe²⁺ and Fe³⁺ on the surface of the catalysts. The contradictory results of XRD and XPS might be the results of surface sensitivity of XPS characterization. We hypothesized that more oxidized species are present on the surface of Mn/Zn-doped ferrites than pure ferrite, and the core part of pure ferrite is more oxidized than Mn/Zn-doped ferrites. a topic we will explore further in the following discussion.

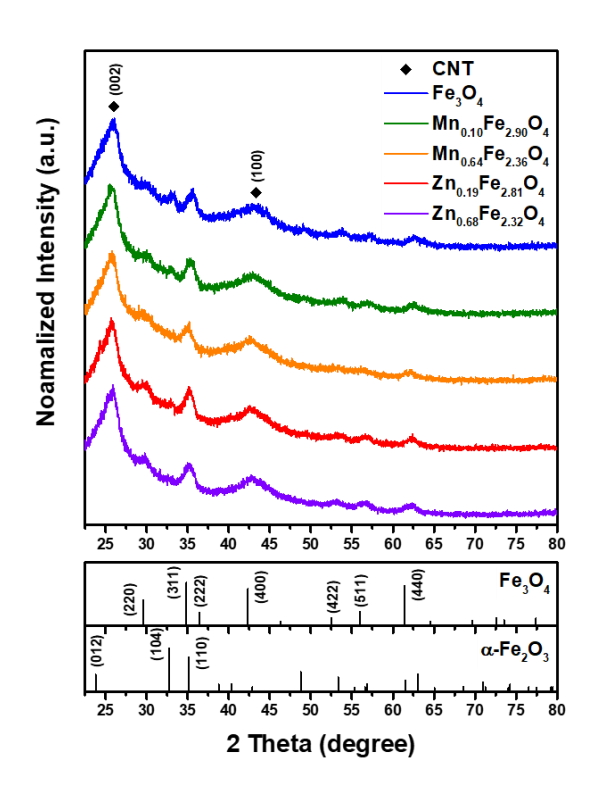


Fig. 2. XRD spectra of Fe₃O₄, Mn_{0.10}Fe_{2.90}O₄, Mn_{0.64}Fe_{2.36}O₄, Zn_{0.19}Fe_{2.81}O₄, and Zn_{0.68}Fe_{2.32}O₄ particles supported on CNT.

The catalytic performance was investigated within a custom-designed reactor operating at 300 °C and 6 bar, using a CO₂/H₂ mixture in a 1:3 ratio. Prior to commencing the CO₂ hydrogenation reaction, the catalysts were reduced in pure H₂ gas to 400 °C. The Fe₃O₄ catalyst achieved a CO₂ conversion of 19 %, yielding primarily CO as the main product (Fig. 3a). The selectivity toward light hydrocarbons (C₂₊) was ~8 %. Upon introducing a minor quantity of manganese additive to the ferrite catalyst (Mn_{0.10}Fe_{2.90}O₄/CNT), the CO₂ conversion was reduced to 11 %, coupled with an increase in the CO selectivity to 78 %. Upon further increasing the Mn amount in the catalyst (Mn_{0.64}Fe_{2.36}O₄/CNT), the catalyst exhibited negligible improvement in activity (Fig. 3a). Consequently, the impact of manganese additives on catalytic performance was not particularly pronounced. Conversely, the influence of the Zn promoter was much more evident. The incorporation of a small quantity of Zn into the ferrite catalyst to form the Zn_{0.19}Fe_{2.81}O₄/CNT sample significantly increased CO₂ conversion (29 %) and selectivity toward C₂₊ hydrocarbons (12 %), while concurrently suppressing CO formation. Among all the tested samples, this catalyst demonstrated the most improved performance in terms of conversion and selectivity. Notably, further increasing the quantity of zinc did not yield enhanced reactivity compared to the ferrite reference material. As depicted in Fig. 3a, the Zn_{0.68}Fe_{2.32}O₄/CNT sample revealed slightly lower CO₂ conversion and C₂₊ production as compared with bare Fe₃O₄. This outcome unequivocally underscores that the precise modulation of the ferrite structure through zinc addition is pivotal in conferring the desired reactivity.

The impact of the support was explored for the most active sample (Zn_{0.19}Fe_{2.81}O₄), utilizing the colloidal approach, which enabled us to transfer the same particles onto a distinct support—Al₂O₃. The Zn_{0.19}Fe_{2.81}O₄/Al₂O₃ catalyst with a low weight loading (0.5 wt. %) demonstrated limited CO₂ conversion (2 %) and marginal C₂₊ selectivity (1 %) (Fig. S3). Increasing the weight loading to 3 wt. % did not enhance the activity. Evidently, the support played a substantial role in influencing the performance, especially considering that the active phase stemmed from the same nanocrystal batch. In a preceding

study, Kim *et al.* analyzed cobalt ferrite catalysts on Al₂O₃, TiO₂, and CNT supports for CO₂ hydrogenation. Only the CNT-supported samples generated iron carbide species, which were acknowledged as active sites responsible for the elevated selectivity towards C₂₊ hydrocarbons. These findings strongly imply that the CNT support played a pivotal role in facilitating highly effective carburization of the oxide phase and achievement of optimal CO₂ hydrogenation activity. It is reasonable to assume that a similar effect was also present in our catalysts. In addition, we tested the activity and selectivity of CNT under reaction conditions. Low CO₂ conversion (0.1 %) and high selectivity toward CO (75 %) and CH₄ (25 %) were observed (Fig. S4). This result demonstrated that the origin of high selectivity and conversion of catalysts with CNT supports is the interaction between ferrites and CNT, not from the CNT support itself.

The CO₂ hydrogenation performance difference in the library of ferrite catalysts that we prepared was more pronounced when the catalytic activity was normalized in terms of Fe time yield (FTY), which assumes that Fe species are the dominant active sites for the reaction and that the Mn and Zn promoters only modify the activity of the Fe but are not themselves active (Fig. 3b). The CNT-supported Fe₃O₄ sample exhibited FTY values for CO₂ conversion and C₂₊ production of 79 and 6.1 μmol_{CO₂} g_{Fe}-1 s⁻¹, respectively. Upon introducing even small quantities of manganese into the catalyst material, FTY efficiency notably declined. In contrast, the Zn_{0.19}Fe_{2.81}O₄/CNT sample, featuring a low quantity of the Zn promoter, demonstrated an improved FTY for both CO₂ conversion and C₂₊ production, with enhancements of ~2 and 3 times, respectively, compared to Fe₃O₄/CNT. Furthermore, by increasing the zinc content in the catalyst, the Zn_{0.68}Fe_{2.32}O₄/CNT exhibited a CO₂ conversion FTY performance surpassing that of bare Fe₃O₄. This enhancement is underestimated in Fig. 3a due to the relatively lower content of active Fe species present in the Zn_{0.68}Fe_{2.32}O₄/CNT sample. Table S1 presents a selection of representative previous studies related to iron-based catalysts applied in CO₂ hydrogenation under higher

pressure (>10 bar). ^{9,12,29-30} Our Zn_{0.19}Fe_{2.81}O₄/CNT sample demonstrated relatively modest FTY efficiency in C₂₊ production, which could potentially be attributed to the lower working pressure (6 bar), thereby affecting the C-C coupling capability on the catalyst surface. Nevertheless, its FTY for CO₂ conversion surpassed that of most studies, underscoring the crucial role of Zn promoters in iron-based catalysts to enhance the transformation of CO₂ molecules in catalytic processes.

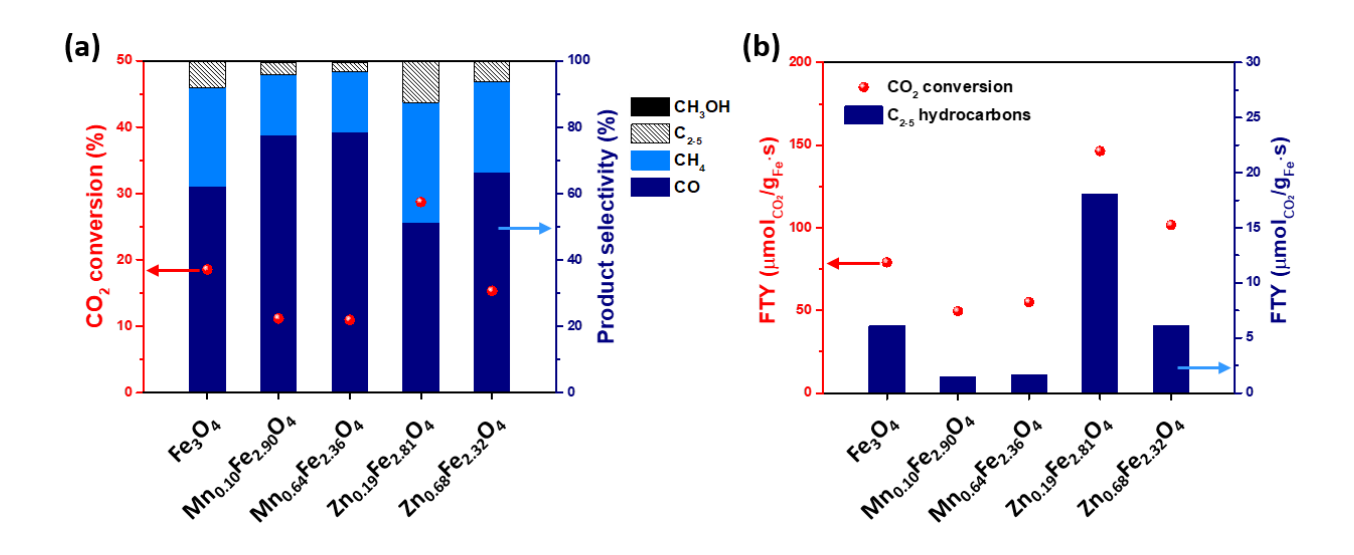


Fig. 3. Catalytic activities of catalyst materials for CO₂ hydrogenation (reaction conditions: CO₂:H₂ = 1:3, WHSV: $6{,}000 \text{ mL} \cdot \text{h}^{-1} \cdot \text{g}_{\text{cat}}^{-1}$, 300 °C, 6 bar). (a) CO₂ conversion and product selectivity Fe₃O₄, Mn_{0.10}Fe_{2.90}O₄, Mn_{0.64}Fe_{2.36}O₄, Zn_{0.19}Fe_{2.81}O₄, and Zn_{0.68}Fe_{2.32}O₄ particles supported on CNT. (b) Fe time yield (FTY) for total CO₂ conversion and conversion to light hydrocarbons (C₂₋₅).

TEM was used to investigate the morphology of the spent catalysts (Fig. 4). While Mn and Zn additives have been recognized as structure stabilizers in iron-based catalysts to mitigate particle sintering during thermocatalytic processes, there have been no reports that precisely compared their efficiencies in

preventing particle aggregation. In the case of Fe₃O₄/CNT, after undergoing CO₂ hydrogenation, the particle size dramatically increased to over 20 nm (Fig. 4a-b). Intriguingly, with the incorporation of trace amounts of manganese into the Fe₃O₄ catalyst (Mn_{0.10}Fe_{2.90}O₄/CNT), the observed maximum particle size after catalysis did not exceed 20 nm (Fig. 4c-d). Furthermore, Mn_{0.64}Fe_{2.36}O₄/CNT exhibited even better performance in reducing particle sintering, resulting in most catalyst particles being smaller than 15 nm after catalysis (Fig. 4e-f). On the other hand, upon introducing a small quantity of zinc into the iron catalyst (Zn_{0.19}Fe_{2.81}O₄/CNT), the maximum particle size increased to ~19 nm (Fig. 4g-h). Additionally, this sample exhibited a predominant particle size distribution ranging from 10 to 13 nm, which differed from the catalyst with Mn additives (Fig. 4c-d). The spent Zn_{0.68}Fe_{2.32}O₄/CNT catalyst, containing higher amounts of the Zn promoter, displayed a slightly improved capability in preventing particle aggregation (Fig. 4i-j). Although the Zn additive may not be as effective as the Mn promoter in inhibiting sintering, it is important to note that the average particle size of the spent catalysts (ferrite: 12.8 nm, Zn_{0.19}Fe_{2.81}O₄: 11.2 nm, Zn_{0.68}Fe_{2.32}O₄: 9.7 nm) clearly indicates that the addition of Zn resulted in a smaller increase in particle size after the reaction compared to the pure ferrite catalysts. This observation suggests that the potential introduction of both Mn and Zn additives in the appropriate amounts could lead to reduced particle sintering and improved catalytic performance.

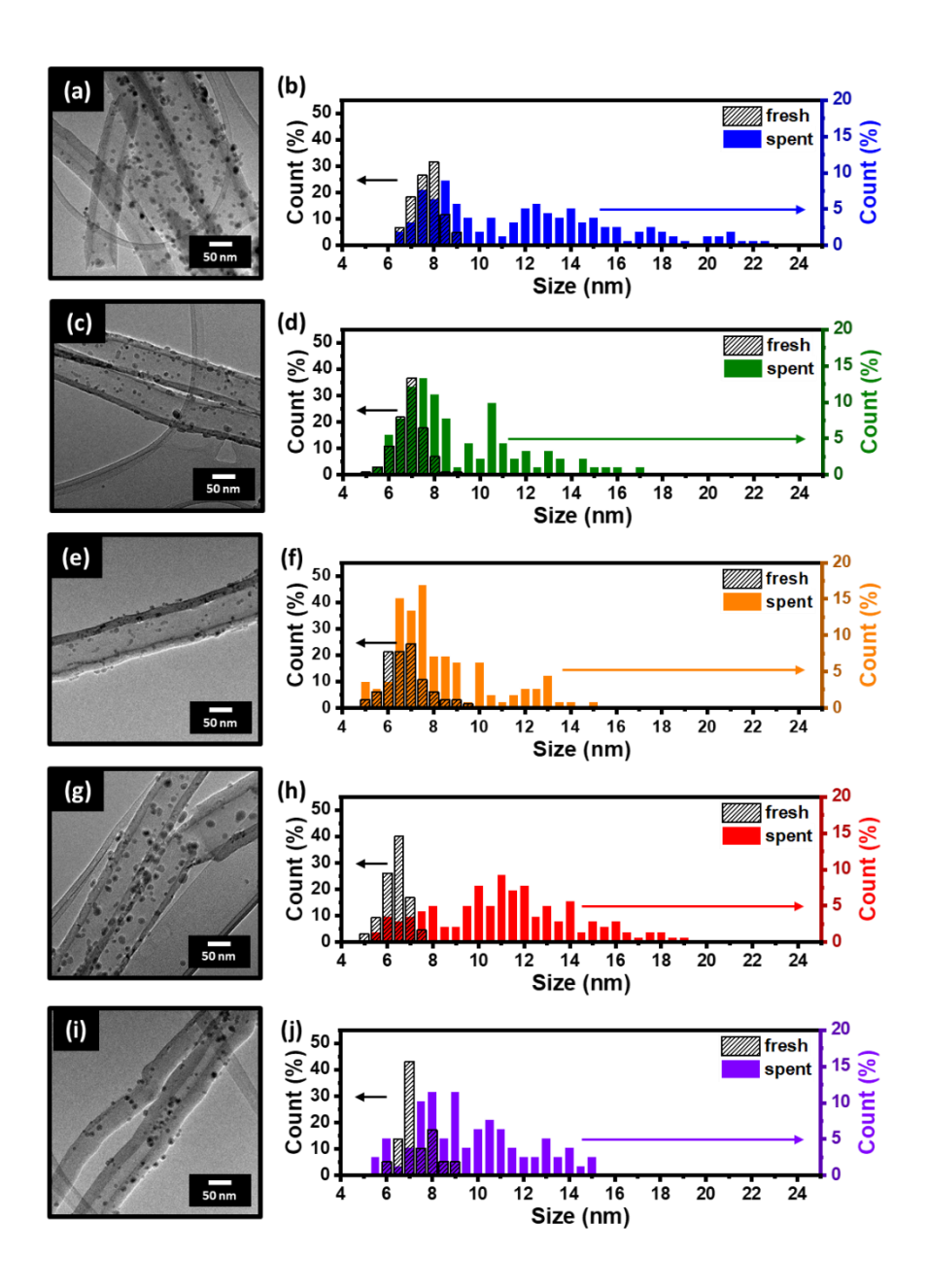


Fig. 4. TEM images and particle size distributions of spent (a,b) Fe₃O₄, (c,d) Mn_{0.10}Fe_{2.90}O₄, (e,f) Mn_{0.64}Fe_{2.36}O₄, (g,h) Zn_{0.19}Fe_{2.81}O₄, and (i,j) Zn_{0.68}Fe_{2.32}O₄ catalysts supported on CNT.

Based on the TEM results, it is evident that both manganese and zinc additives effectively mitigate catalyst sintering, resulting in smaller particle sizes after CO₂ hydrogenation. Smaller particle sizes lead

to higher surface areas, which in turn can contribute to increase catalytic rates. However, among the samples with additives, only the Fe₃O₄ catalyst with Zn promoters displayed improved FTY efficiency compared to bare Fe₃O₄ (Fig. 3b). To explore the underlying reasons, XRD spectra were also employed to analyze the spent catalyst materials (Fig. 5). Following CO₂ hydrogenation, aside from the diffraction peaks originating from the CNT supports, the peaks corresponding to the initial iron oxide phases in the Fe₃O₄/CNT sample diminished. Intriguingly, a broad band emerged around a 2 θ value of 45°, potentially indicating the presence of α -Fe and Fe₅C₂ phases. We hypothesized that these metallic and carbide components in the spent catalyst might have resulted from the reducing atmosphere and reaction of the oxide precursor with dissociated carbon species during CO₂ hydrogenation catalysis. Particularly noteworthy is the Fe₅C₂ phase, recognized as an active site for hydrocarbon generation. ¹⁴⁻¹⁵

It is intriguing to observe that the peak at the 2θ value of 45° was much less pronounced in samples with Mn additives. We speculate that the stronger intensity of this diffraction peak in the XRD pattern of the spent catalysts could be attributed to their enhanced reducibility. Both Mn_{0.10}Fe_{2.90}O₄/CNT and Mn_{0.64}Fe_{2.36}O₄/CNT appeared to be less reducible, and that the carburization of the oxide phase was not as pronounced, hindering the formation of catalytic species essential for producing C₂₊ products and resulting in comparatively lower FTY performance (Fig. 3b). It is worth noting that some previous works reported better efficiency of iron-based catalysts prepared through conventional methods when manganese was introduced. ^{17,31} We posit that these conventional preparations often alter multiple parameters (such as particle size, size distribution, and composition), which might lead to a potentially misleading assessment of performance improvements attributed to Mn additives. Moreover, the CO₂ hydrogenation performance in previous studies was conducted at high working pressures, exacerbating particle sintering. ¹⁷ Consequently, under this operational condition, the structure stabilizing effect of manganese on the catalyst structure might prove more effective in retaining surface area to achieve higher activity. In our

work, the introduction of Zn promoters led the spent catalysts to exhibit a strong diffraction peak corresponding to α -Fe and Fe₅C₂ phases (Fig. 5), ultimately resulting in superior FTY efficiency compared to other samples (Fig. 3b).

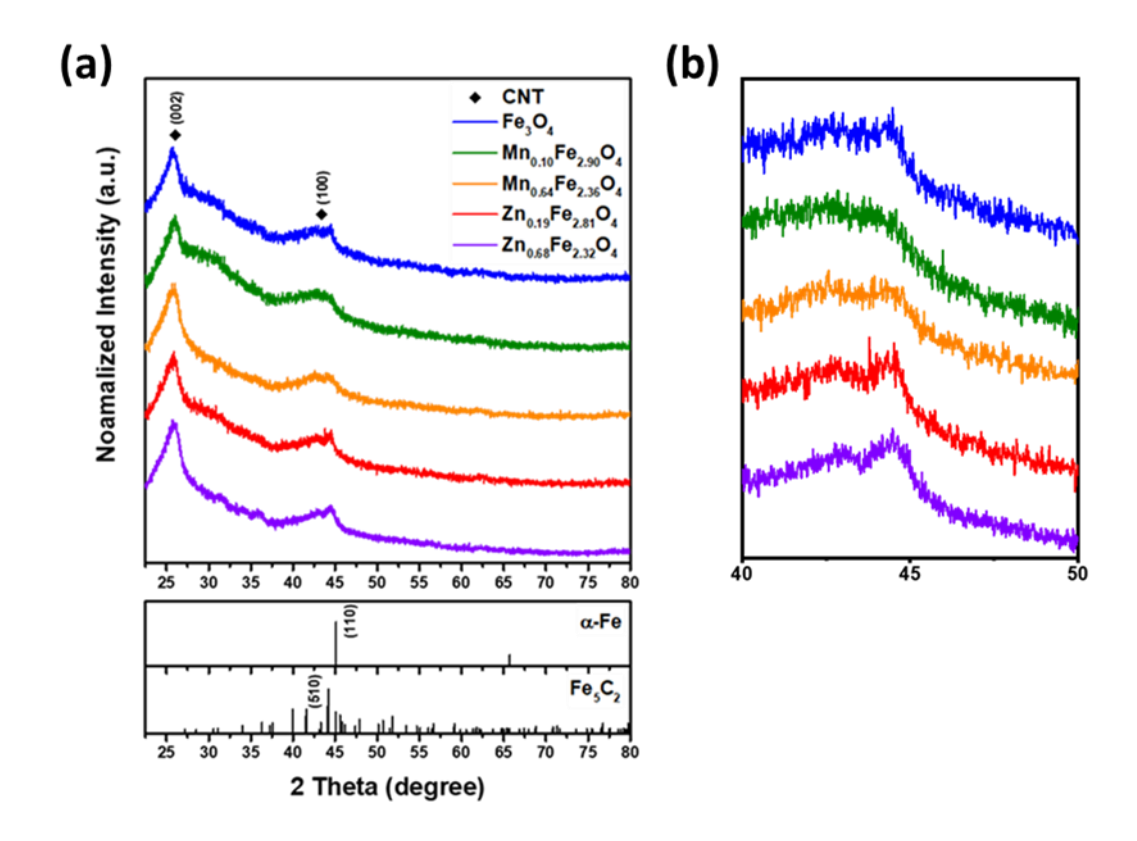


Fig. 5. (a) XRD patterns of spent Fe₃O₄, Mn_{0.10}Fe_{2.90}O₄, Mn_{0.64}Fe_{2.36}O₄, Zn_{0.19}Fe_{2.81}O₄, and Zn_{0.68}Fe_{2.32}O₄ catalysts supported on CNT. (b) Enlarged image of peaks around 45°.

4. Conclusions

This study explored the catalytic capabilities of ferrite colloidal nanocrystals in CO₂ hydrogenation, with a particular focus on the influence of manganese and zinc additives. Employing

controlled synthesis techniques, the research investigated the impact of specific parameters on catalytic

performance. The findings revealed that both Mn and Zn additives played a crucial role in mitigating

catalyst sintering, resulting in the preservation of smaller particle sizes following catalytic reaction.

Interestingly, while manganese additives effectively stabilized the catalyst structure and suppressed

sintering, their contribution to promoting the CO₂ hydrogenation process was not evident. Consequently,

the resulting CO₂ conversion and selectivity toward C₂₊ hydrocarbons were decreased compared to the

bare ferrite catalyst. Notably, the introduction of trace amounts of zinc instead emerged as a pivotal factor

that significantly enhanced both catalytic activity and selectivity. This improvement was attributed to the

heightened reducibility and carburization efficiency of the catalyst, which in turn facilitated the generation

of active catalytic species essential to produce desired C_{2+} products.

AUTHOR INFORMATION

*Corresponding Authors:

* E-mail: mcargnello@stanford.edu (M. Cargnello) Tel: +1-650-7246422

Supporting Information

Additional information about additional tables. This material is available free of charge via the Internet at

http://www.sciencedirect.com.

Acknowledgments

This research was supported by the National Science and Technology Council (NSTC) in Taiwan

through the Stanford-Taiwan LEAP program administered by National Applied Research Laboratories

21

(NARLabs). Additional support was provided by the National Science Foundation under grant 1956300 (J.O.). C.-J. Chen expresses gratitude to the NARLabs of Taiwan for the visiting scholar fellowship. Part of this work was performed at the Stanford Nano Shared Facilities (SNSF), supported by the National Science Foundation under award ECCS-2026822.

References

- 1. Li, C.; Wang, T.; Liu, B.; Chen, M.; Li, A.; Zhang, G.; Du, M.; Wang, H.; Liu, S. F.; Gong, J., Photoelectrochemical CO2 reduction to adjustable syngas on grain-boundary-mediated a-Si/TiO2/Au photocathodes with low onset potentials. *Energy & Environmental Science* **2019**, *12*, 923-928.
- 2. Brethomé, F. M.; Williams, N. J.; Seipp, C. A.; Kidder, M. K.; Custelcean, R., Direct air capture of CO2 via aqueous-phase absorption and crystalline-phase release using concentrated solar power. *Nature Energy* **2018**, *3*, 553-559.
- 3. Ye, R.-P.; Ding, J.; Gong, W.; Argyle, M. D.; Zhong, Q.; Wang, Y.; Russell, C. K.; Xu, Z.; Russell, A. G.; Li, Q.; Fan, M.; Yao, Y.-G., CO2 hydrogenation to high-value products via heterogeneous catalysis. *Nature Communications* **2019**, *10*, 5698.
- 4. Zhang, J.; Lu, S.; Su, X.; Fan, S.; Ma, Q.; Zhao, T., Selective formation of light olefins from CO2 hydrogenation over Fe–Zn–K catalysts. *Journal of CO2 Utilization* **2015**, *12*, 95-100.
- 5. Li, Y.; Gao, W.; Peng, M.; Zhang, J.; Sun, J.; Xu, Y.; Hong, S.; Liu, X.; Liu, X.; Wei, M.; Zhang, B.; Ma, D., Interfacial Fe5C2-Cu catalysts toward low-pressure syngas conversion to long-chain alcohols. *Nature Communications* **2020**, *11*, 61.
- 6. Aitbekova, A.; Goodman, E. D.; Wu, L.; Boubnov, A.; Hoffman, A. S.; Genc, A.; Cheng, H.; Casalena, L.; Bare, S. R.; Cargnello, M., Engineering of Ruthenium–Iron Oxide Colloidal Heterostructures: Improved Yields in CO2 Hydrogenation to Hydrocarbons. *Angewandte Chemie International Edition* **2019**, *58*, 17451-17457.
- 7. Torres Galvis, H. M.; de Jong, K. P., Catalysts for Production of Lower Olefins from Synthesis Gas: A Review. *ACS Catalysis* **2013**, *3*, 2130-2149.
- 8. Wei, J.; Ge, Q.; Yao, R.; Wen, Z.; Fang, C.; Guo, L.; Xu, H.; Sun, J., Directly converting CO2 into a gasoline fuel. *Nature Communications* **2017**, *8*, 15174.
- 9. Wang, S.; Wu, T.; Lin, J.; Ji, Y.; Yan, S.; Pei, Y.; Xie, S.; Zong, B.; Qiao, M., Iron–Potassium on Single-Walled Carbon Nanotubes as Efficient Catalyst for CO2 Hydrogenation to Heavy Olefins. *ACS Catalysis* **2020**, *10*, 6389-6401.
- 10. Cui, X.; Gao, P.; Li, S.; Yang, C.; Liu, Z.; Wang, H.; Zhong, L.; Sun, Y., Selective Production of Aromatics Directly from Carbon Dioxide Hydrogenation. *ACS Catalysis* **2019**, *9*, 3866-3876.
- 11. Yang, C.; Zhao, B.; Gao, R.; Yao, S.; Zhai, P.; Li, S.; Yu, J.; Hou, Y.; Ma, D., Construction of Synergistic Fe5C2/Co Heterostructured Nanoparticles as an Enhanced Low Temperature Fischer–Tropsch Synthesis Catalyst. *ACS Catalysis* **2017**, *7*, 5661-5667.
- 12. Kim, K. Y.; Lee, H.; Noh, W. Y.; Shin, J.; Han, S. J.; Kim, S. K.; An, K.; Lee, J. S., Cobalt Ferrite Nanoparticles to Form a Catalytic Co–Fe Alloy Carbide Phase for Selective CO2 Hydrogenation to Light Olefins. *ACS Catalysis* **2020**, *10*, 8660-8671.

- 13. Zhang, Y.; Fu, D.; Liu, X.; Zhang, Z.; Zhang, C.; Shi, B.; Xu, J.; Han, Y.-F., Operando Spectroscopic Study of Dynamic Structure of Iron Oxide Catalysts during CO2 Hydrogenation. *ChemCatChem* **2018**, *10*, 1272-1276.
- 14. Chang, Q.; Zhang, C.; Liu, C.; Wei, Y.; Cheruvathur, A. V.; Dugulan, A. I.; Niemantsverdriet, J. W.; Liu, X.; He, Y.; Qing, M.; Zheng, L.; Yun, Y.; Yang, Y.; Li, Y., Relationship between Iron Carbide Phases (ε-Fe2C, Fe7C3, and χ-Fe5C2) and Catalytic Performances of Fe/SiO2 Fischer—Tropsch Catalysts. *ACS Catalysis* **2018**, *8*, 3304-3316.
- 15. Park, H.; Youn, D. H.; Kim, J. Y.; Kim, W. Y.; Choi, Y. H.; Lee, Y. H.; Choi, S. H.; Lee, J. S., Selective Formation of Hägg Iron Carbide with g-C3N4 as a Sacrificial Support for Highly Active Fischer–Tropsch Synthesis. *ChemCatChem* **2015**, *7*, 3488-3494.
- 16. Liang, B.; Sun, T.; Ma, J.; Duan, H.; Li, L.; Yang, X.; Zhang, Y.; Su, X.; Huang, Y.; Zhang, T., Mn decorated Na/Fe catalysts for CO2 hydrogenation to light olefins. *Catalysis Science & Technology* **2019**, *9*, 456-464.
- 17. Xu, Y.; Zhai, P.; Deng, Y.; Xie, J.; Liu, X.; Wang, S.; Ma, D., Highly Selective Olefin Production from CO2 Hydrogenation on Iron Catalysts: A Subtle Synergy between Manganese and Sodium Additives. *Angewandte Chemie International Edition* **2020**, *59*, 21736-21744.
- 18. Choi, Y. H.; Ra, E. C.; Kim, E. H.; Kim, K. Y.; Jang, Y. J.; Kang, K.-N.; Choi, S. H.; Jang, J.-H.; Lee, J. S., Sodium-Containing Spinel Zinc Ferrite as a Catalyst Precursor for the Selective Synthesis of Liquid Hydrocarbon Fuels. *ChemSusChem* **2017**, *10*, 4764-4770.
- 19. Zhai, P.; Xu, C.; Gao, R.; Liu, X.; Li, M.; Li, W.; Fu, X.; Jia, C.; Xie, J.; Zhao, M.; Wang, X.; Li, Y.-W.; Zhang, Q.; Wen, X.-D.; Ma, D., Highly Tunable Selectivity for Syngas-Derived Alkenes over Zinc and Sodium-Modulated Fe5C2 Catalyst. *Angewandte Chemie International Edition* **2016**, *55*, 9902-9907.
- 20. Li, S.; Li, A.; Krishnamoorthy, S.; Iglesia, E., Effects of Zn, Cu, and K Promoters on the Structure and on the Reduction, Carburization, and Catalytic Behavior of Iron-Based Fischer–Tropsch Synthesis Catalysts. *Catalysis Letters* **2001**, *77*, 197-205.
- 21. Sharma, P.; Elder, T.; Groom, L. H.; Spivey, J. J., Effect of Structural Promoters on Fe-Based Fischer–Tropsch Synthesis of Biomass Derived Syngas. *Topics in Catalysis* **2014**, *57*, 526-537.
- 22. Cargnello, M., Colloidal Nanocrystals as Building Blocks for Well-Defined Heterogeneous Catalysts. *Chemistry of Materials* **2019**, *31*, 576-596.
- 23. Li, D.; Yun, H.; Diroll, B. T.; Doan-Nguyen, V. V. T.; Kikkawa, J. M.; Murray, C. B., Synthesis and Size-Selective Precipitation of Monodisperse Nonstoichiometric MxFe3–xO4 (M = Mn, Co) Nanocrystals and Their DC and AC Magnetic Properties. *Chemistry of Materials* **2016**, *28*, 480-489.
- 24. Casavola, M.; Hermannsdörfer, J.; de Jonge, N.; Dugulan, A. I.; de Jong, K. P., Fabrication of Fischer–Tropsch Catalysts by Deposition of Iron Nanocrystals on Carbon Nanotubes. **2015**, *25*, 5309-5319.
- 25. Casavola, M.; Xie, J.; Meeldijk, J. D.; Krans, N. A.; Goryachev, A.; Hofmann, J. P.; Dugulan, A. I.; de Jong, K. P., Promoted Iron Nanocrystals Obtained via Ligand Exchange as Active and Selective Catalysts for Synthesis Gas Conversion. *ACS Catalysis* **2017**, *7*, 5121-5128.
- 26. Cargnello, M.; Chen, C.; Diroll, B. T.; Doan-Nguyen, V. V. T.; Gorte, R. J.; Murray, C. B., Efficient Removal of Organic Ligands from Supported Nanocrystals by Fast Thermal Annealing Enables Catalytic Studies on Well-Defined Active Phases. *Journal of the American Chemical Society* **2015**, *137*, 6906-6911.
- 27. Hassinen, A.; Moreels, I.; De Nolf, K.; Smet, P. F.; Martins, J. C.; Hens, Z., Short-Chain Alcohols Strip X-Type Ligands and Quench the Luminescence of PbSe and CdSe Quantum Dots, Acetonitrile Does Not. *Journal of the American Chemical Society* **2012**, *134*, 20705-20712.

- 28. Weidman, M. C.; Beck, M. E.; Hoffman, R. S.; Prins, F.; Tisdale, W. A., Monodisperse, Air-Stable PbS Nanocrystals via Precursor Stoichiometry Control. *ACS Nano* **2014**, *8*, 6363-6371.
- 29. Wu, T.; Lin, J.; Cheng, Y.; Tian, J.; Wang, S.; Xie, S.; Pei, Y.; Yan, S.; Qiao, M.; Xu, H.; Zong, B., Porous Graphene-Confined Fe–K as Highly Efficient Catalyst for CO2 Direct Hydrogenation to Light Olefins. *ACS Applied Materials & Interfaces* **2018**, *10*, 23439-23443.
- 30. Elishav, O.; Shener, Y.; Beilin, V.; Landau, M. V.; Herskowitz, M.; Shter, G. E.; Grader, G. S., Electrospun Fe–Al–O Nanobelts for Selective CO2 Hydrogenation to Light Olefins. *ACS Applied Materials & Interfaces* **2020**, *12*, 24855-24867.
- 31. Liu, B.; Geng, S.; Zheng, J.; Jia, X.; Jiang, F.; Liu, X., Unravelling the New Roles of Na and Mn Promoter in CO2 Hydrogenation over Fe3O4-Based Catalysts for Enhanced Selectivity to Light α-Olefins. *ChemCatChem* **2018**, *10*, 4718-4732.

Graphical Abstract

